Journal of Materials Chemistry A

ROYAL SOCIETY OF CHEMISTRY

PAPER

View Article Online
View Journal

Cite this: DOI: 10.1039/d5ta04494d

Dual alkali-carbonate activated nitrogen-doped carbons as oxygen reduction reaction electrocatalysts: a study of porosity structure effects

Lettie A. Smith,[a] J. Ehren Eichler,[a] Kenta Kawashima,[a] Hanah Leonard,[b] Franklin Tang,[c] Ethan Kang Yang,[a] Wuilian A. Martinez,[a] Yasaman Karbalaeemorad[a] and C. Buddie Mullins *[acdef]

Nitrogen-doped carbons with consistent N-content and N-functionality distribution but variable porosity and surface area were prepared and studied to evaluate textural property effects on oxygen reduction reaction (ORR) electrocatalysis independent of chemical composition. By employing various characterization techniques, the similar N-content (1–2.5 at%) and N-motif distribution were confirmed between samples, as was variability in porosity and surface area. From electrochemical testing, a larger micropore volume associated with pores < 1 nm (>0.25 $cm^3\ g^{-1}$) and surface area (>approximately 1000 $m^2\ g^{-1}$) correlated with increased onset potential (E_{onset}), half-wave potential ($E_{1/2}$), and an electron transfer number, n, of approximately 4, wherein the most significant effect of porous structure on electrochemical performance was observed for $E_{1/2}$. With respect to E_{onset} and n, more subtle effects were observed regarding micropore volume (<1 nm) and surface area, as the kinetics of the ORR are predominantly tuned by the presence and type of active N-sites. An increased micropore volume and surface area realized slight increases in E_{onset} and n owing to improved access to these active sites. Thus, textural properties primarily affect mass transport for ORR electrocatalysis with effects on kinetic parameters only arising regarding accessibility to active sites located within micropores.

Received 3rd June 2025
Accepted 22nd July 2025

DOI: 10.1039/d5ta04494d

rsc.li/materials-a

Introduction

With the increased demand to diversify the world's energy supply, the need to develop green technologies such as fuel cells becomes more and more urgent. Fuel cells utilizing either hydrogen or methanol offer a low-carbon emission, sustainable means for large-scale energy conversion and storage applications. Specifically, they could help increase the proportion of renewable energy used in the transportation sector, wherein only 4% of energy demand is currently met using renewables,[1] by replacing traditional internal combustion engines. Batteries have so far predominated in this space, however, unlike batteries, fuel cells offer reduced recharge times and longer lifespans (depending on the duration of use). In comparison to conventional engines, fuel cells also tout higher energy efficiency, sometimes achieving 50% efficiency in contrast to the 20% efficiency of non-diesel internal combustion engines.[2] Despite these advantages, fuel cells have not undergone widespread implementation because of issues with durability, reliability, and cost.[2,3] The electrodes in fuel cells typically contain Pt-based materials that act as electrocatalysts to overcome the sluggish kinetics of the redox reactions that enable energy conversion in fuel cell(s). Because Pt, a rare earth metal, is required, it drives up the cost to produce these devices. These Pt-based electrodes are also subject to poor durability, especially in regard to direct methanol fuel cells wherein methanol crossover from the anode to the cathode presents a huge problem.[4,5]

For the oxygen reduction reaction (ORR), one of the half-reactions in both direct methanol fuel cells and hydrogen fuel cells, porous and doped carbon materials have emerged as a replacement for these Pt-based materials.[6–8] These carbon materials have demonstrated similar performance to platinum on carbon (Pt/C) with improved durability.[6,9–12] For example, Lv and coworkers were able to obtain a half-wave potential ($E_{1/2}$) of 0.85 V *vs.* the reversible hydrogen electrode (RHE) with their N-doped hydrogen-substituted graphdiyne prepared at 900 °C, rivaling that of platinum on carbon. Additionally, their carbon

[a]Department of Chemistry, The University of Texas at Austin, Austin, TX 78712, USA
[b]Department of Biochemistry, The University of Texas at Austin, Austin, TX 78712, USA
[c]John J. McKetta Department of Chemical Engineering, The University of Texas at Austin, Austin, TX, 78712, USA
[d]Texas Materials Institute, The University of Texas at Austin, Austin, TX 78712, USA
[e]Allen J. Bard Center for Electrochemistry, The University of Texas at Austin, Austin, TX 78712, USA
[f]H2@UT, The University of Texas at Austin, Austin, TX 78712, USA

material had high selectivity with an electron transfer number, n, of approximately 4 and superior resistance to methanol crossover in comparison to Pt/C.[13] The superior performance of the hydrogen-substituted graphdiyne was attributed to a large Brunauer–Emmett–Teller (BET) surface area (SA) at 1754 $m^2 g^{-1}$ and an abundance of pyridinic-N sites (only pyridinic N present at 2.9 ± 0.3 at%). As indicated by Lv *et al.*'s work, the porous structure and N motifs of N-doped carbons are considered the driving force behind their ORR electrocatalytic performance. An increased surface area has been attributed to an increased number of exposed active sites and improved mass transfer.[14] The type of N groups in the carbon matrix have also been ascribed to improved $E_{1/2}$ and selectivity, n, for the 4 *vs.* 2-electron pathway of the ORR (producing either water or hydrogen peroxide, respectively).[9,10,13,15–19] Of the typical N sites detected in these carbon materials, graphitic, pyrrolic, and pyridinic N have been attributed to selectivity for the 4-electron pathway.[9–12,16,20–22] These N-motifs are thought to increase performance by inducing a partial positive charge at adjacent carbon atoms, promoting the adsorption of oxygen.[18,23,24]

The extent to which porous structure, total N-content, and N composition affect the electrocatalytic performance of N-doped carbons independently is, however, difficult to gauge as both of these parameters tend to change simultaneously. Ferrero *et al.* investigated the role of pore size distribution at a constant N-content and N-distribution by using silica templates to obtain microporous and mesoporous N-doped carbon microspheres using pyrrole as a N precursor (difference in mesopore volume of 1.13 $cm^3 g^{-1}$ with all other adsorption parameters of nearly the same value).[12] They found that the microspheres consisting mainly of mesopores exhibited better activity and selectivity for the 4-electron pathway of the ORR. However, these differences in performance were slight with $E_{1/2}$-values at nearly the same potential and the onset potential (E_{onset}) only differing by ~20 mV between the microporous and mesoporous microspheres.

Similarly, Dai and coworkers attributed micropores to reduced ORR performance for N-doped carbons.[25] They concluded that micropores detracted from the ORR activity of their prepared carbons because such small pores were kinetically inaccessible to O_2. Rather, improvements with ORR performance correlated with increases in mesopore volume, as indicated by Lv *et al.* above and others.[13,26,27] Alternatively, Yao and coworkers,[28] Eisenberg and coworkers,[29] and Zhang and coworkers[30] found that microporosity had a positive effect on ORR electrocatalysis, enabling a greater number of exposed active sites for electrocatalysis and improved mass transport when present in addition to mesopores in the N-doped carbon porous network.

An additional study analyzing oxidized carbons (N-free) alongside N-doped and oxidized carbons (1.4–2.1 at% N) found that N-free samples demonstrated superior performance owing to an abundance of smaller diameter micropores, as compared to the N-doped samples. Specifically, the oxidized, N-free samples predominately consisted of micropores 0.37 nm in size, close in size to that of an O_2 molecule with a kinematic diameter of 0.346 nm.[31] The authors proposed that these small micropores participated in and promoted the ORR because of a hierarchical porous network containing oxygen-containing functional groups in larger pores that enabled electrolyte penetration up to small micropores. They hypothesized that these micropores did not contain oxygen groups and were hydrophobic in nature, allowing extraction of O_2 from the electrolyte, wherein O_2 solubility is quite low.[32] The highly confining pore geometry of this active site was speculated to reduce O_2 to OH^- *via* a 2-step 2-electron reduction pathway. Further evidence of this small micropore effect is provided by Gabe and coworkers, who studied porous carbon containing only C and O.[33] They developed a model taking into account narrow and wide micropores, mass transport of O_2 and HO_2^- through said pores, and the charge transfer of each reaction pathway involved in the ORR. From their modeling and experimental results, they were able to determine that micropores contribute to the ORR, that narrow micropores promote O_2 reduction to HO_2^-, and that the rate of HO_2^- diffusion is suppressed such that the reduction of HO_2^- to OH^- is favored. Thus, in the absence of N-doping, narrow micropores promote a 2-step 2-electron reduction of O_2 to OH^- rather than direct 4-electron reduction.

Despite the findings on micropore effects on ORR electrocatalysis for porous carbons containing oxygen functional groups, the role of micropores with respect to N-doped, porous carbons is still unclear. As discussed above and in a recent review paper,[23] there exist conflicting reports on the impact of micropores on electrocatalysis in conjunction with N-sites both in terms of total N-content and the predominant N-motif. Thus, there is room for further exploration of the role of porous structure on ORR electrocatalysis for N-doped carbon electrocatalysts.

Herein, the effect of porous structure on N-doped carbon performance and selectivity as ORR electrocatalysts is investigated independent from the N-content by leveraging a synthetic method that imparts pore tunability while maintaining consistent N-content. Specifically, a N-doped carbon foam was chemically activated at 1000 °C following a dual-cation procedure enlisting the activators Na_2CO_3 and K_2CO_3.[34,35] In brief, the total N-content was controlled by the activator : N precursor and the N : C precursor ratios.[35] Then, by varying the mole fraction of the activating mixture (Na_2CO_3 and K_2CO_3), the N-content was maintained while porosity was modulated significantly. Specifically, increasing the mol fraction of Na_2CO_3 to K_2CO_3 led to a more restricted porous network, reduced porosity (0.45 *vs.* ~0.60 $cm^3 g^{-1}$), and smaller surface area (772.7 *vs.* 1202.4 $m^2 g^{-1}$).

Electrochemical testing of the porous, N-doped carbons revealed that improved performance and selectivity were observed when a K_2CO_3-rich activating mixture was employed. The N-doped carbons prepared with a greater proportion of K_2CO_3 *vs.* Na_2CO_3, exhibited larger $E_{1/2}$ and E_{onset}. The improved $E_{1/2}$ of the K_2CO_3-rich carbons was attributed to increased surface area and micropore volumes, as compared to the carbons prepared with Na_2CO_3-rich activation mixtures. The larger surface areas and micropore volumes of the K_2CO_3-rich activated carbons led to improved mass transport such that $E_{1/2}$ increased. The large surface areas and micropore volumes of the K_2CO_3-rich activated carbons also led to increased E_{onset}, as

a more open porous structure led to improved access to active sites for catalysis, indicating a slight effect of porosity on kinetics of the ORR. Concerning selectivity, n, a meaningful difference was only observed between the N-doped carbons prepared with a proportion of or 100% K_2CO_3 *vs.* the 100% Na_2CO_3 sample, as the latter resulted in a more tortuous porous network, restricting access of reactants to active sites for electrocatalysis. Thus, the volume of micropores tunes both E_{onset} and $E_{1/2}$, with an abundance of micropores leading to improved performance. A large micropore volume and, as a result, a large surface area were obtained by employing a more K_2CO_3-rich activating mixture at 1000 °C. In addition, a K_2CO_3-rich mixture also led to increased selectivity (~4 electrons), owing to improved access to active sites *via* an interconnected, open pore network and large surface area.

Experimental

Chemicals

All chemicals were of analytical grade unless otherwise noted and were used as received. Sucrose was obtained from Alfa Aesar (99%). Melamine was obtained from Sigma Aldrich (99%). Potassium hydroxide was obtained from Sigma Aldrich (KOH, 90%), and hydrochloric acid was obtained from VWR chemicals (HCl, 34–37% w/w). The activators/pore-generating agents, potassium carbonate and sodium carbonate, were obtained from Fisher Scientific. The KOH was used to prepare the electrolyte for electrochemical tests, and hydrochloric acid (HCl) was used to prepare an acid solution (1 M) for sample washing. Ultrapure water (18.2 MΩ cm) was used for sample filtering.

Semi-carbonization of sucrose and melamine

Carbon foams were prepared according to previous work.[36] First, a 20 g sucrose and melamine mixture was prepared by grinding using a mortar and pestle. The sucrose–melamine mixture was 20% sucrose and 80% melamine by mass. This ratio of sucrose to melamine was selected based on past work that indicated carbon foams prepared with 80% melamine resulted in greater pyridinic N content,[36] which has been ascribed to boosted ORR electrocatalytic performance and selectivity for the 4-electron process.[18] After grinding, the mixture was divided evenly into four covered alumina crucibles (250 mL) and heated in air at 410 °C for 2.5 h at a ramp rate of 5 °C min^{-1}. The resulting semi-carbonized foam had a very light and fluffy texture. The foam was then ground into a powder using a mortar and pestle.

Activation of semi-carbonized samples

Activation was performed according to previous work.[36] First, 1.5 g of the semi-carbonized foam was impregnated with 13.35 mL of either 1 M K_2CO_3, 1 M Na_2CO_3, or a mixture of the two (at 25, 50, and 75 mol% Na_2CO_3). The impregnated sample was then dried overnight at 120 °C. Then, the sample was placed in a covered alumina crucible (20 mL) and activated in a tube furnace at 1000 °C (held 60 min, ramp rate of 3 °C min^{-1}) under an Ar atmosphere (flow at 150 sccm). The activated sample was allowed to cool to room temperature naturally and then washed with HCl (1 M, 50 mL) for 1 h. Sample filtration was then performed using two liters of ultrapure water to remove inorganic salts, leaving behind a porous N-doped carbon. In total, five different samples were prepared and are referred to as *X*Na, where *X* is mol% of Na_2CO_3 used for activation which was either 0, 25, 50, 75, or 100.

Material characterization

The (semi)crystallinity of the N-doped carbons was determined with X-ray diffraction (XRD, Rigaku Miniflex 600 Diffractometer II) employed with Cu Kα radiation (λ = 1.5418 Å). Diffraction patterns were collected in continuous mode from 5 to 60° at 2.5° min^{-1} using a crystal Si zero-background diffraction holder (MTI).

The presence of defects within the N-doped carbons was gauged by employing Raman spectroscopy to determine the I_D to I_G ratio. Specifically, a Renishaw *InVia* Raman system with an Ar-ion laser (514 nm, 50 mW) for excitation was focused on the sample using a microscope with a 50× objective lens. Raman spectra were collected from 500 to 3500 cm^{-1} with a laser exposure time of 60 s. The resulting Raman spectra were normalized and fit with six bands with Voigt peak shapes (Fig. S7). These six bands were the D4, D, D3, G, 2D, and G + D bands. The D4 band at ~1200 cm^{-1} and D3 band at ~1500 cm^{-1} have been attributed to amorphous character and vibrations associated with the presence of heteroatoms and other defects.[37,38] The D band at ~1350 cm^{-1} is also related to the presence of defects, such as heteroatom doping, vacancies, and holes. The G-band at ~1580 cm^{-1} is associated with the stretching mode of sp^2 bonded carbon. Then, the 2D and G + D are overtones, representing higher vibrational energy transitions that are multiples of the D and G bands.[39–41] An additional peak, D2 at ~1620 cm^{-1} associated with vibrations due to doping or other impurities, was not included in the fitting as it is associated with graphitic materials, and the carbons studied herein have amorphous characteristics.[37,38]

To observe changes in morphology, scanning electron microscopy (SEM) images were collected with an Apreo S SEM at an accelerating voltage of 10.0–20.0 kV and a beam current of 0.40 nA under vacuum. In addition, scanning transmission electron microscopy (STEM) was performed with a Hitachi S-5500 SEM/STEM to obtain sub-nanometer resolution images with accelerating voltages of 20.0–30.0 kV.

The surface composition of the prepared N-doped carbons was characterized with X-ray photoelectron spectroscopy (XPS, VersaProbe 4 X-ray Photoelectron Spectrometer) using monochromatic Al Kα radiation and by performing analysis with CasaXPS™ software. All spectra were calibrated to the sp^2 carbon (C=C) peak at 284.7 eV and fitted using Gaussian–Lorentzian peaks with Shirley backgrounds. High-resolution C 1s scans were deconvoluted using four peaks at 284.7 eV ± 0.0 (C=C), 285.8 ± 0.1 eV (C=N/C–C), 286.7 ± 0.1 eV (C–N), 289.2 eV ± 0.2 (N–C=O/C=O), and 291.0 ± 0.2 eV (π–π^*). High-resolution N 1s spectra were deconvoluted with four peaks centered at 398.4 ± 0.1 eV (C=N–C), 399.9 ± 0.2 eV (NC_3), 400.9

± 0.1 eV (C_2NH), and 402.3 ± 0.2 eV (NO_x). High-resolution O 1s scans were deconvoluted with two peaks at 533.4 ± 0.2 eV (C=O) and 532.0 ± 0.3 eV (C–O).

The textural properties of the porous, N-doped carbons were determined from N_2 isotherms performed at 77 K using an ASAP 2020 gas analyzer. BET SAs were determined using multi-point BET analysis *via* Micromeritics software. The pore size distributions were determined by the fitting of kernels derived from non-local density functional theory (NLDFT) on graphite. Prior to analysis, the carbon samples were outgassed under vacuum at 200 °C for 12 h.

The fine pore structure (0.3–1.4 nm) of the carbons was further probed by collecting CO_2 isotherms at 0 °C on a Quantachrome Autosorb iQ-MP (Anton Parr). The pore size distributions were determined from these CO_2 isotherms *via* kernels derived from non-local density functional theory (NLDFT) on carbon. To maintain the temperature at 0 °C for isotherm collection, a float sensor with a temperature-controlled glycerol/water bath (Isotemp refrigerated circulator, Fischer Scientific) was employed. Before analysis, all samples were outgassed under vacuum at 200 °C for 12 h.

Electrochemical characterization

Electrochemical measurements were carried out using a rotating ring disk electrode (RRDE, 0.247 cm^2) on a CHI832 bipotentiostat. The catalyst ink was prepared using 5 mg of sample and a 5 wt% Nafion in isopropanol solution (1 mL) and was dropcasted onto the RRDE at a loading of 0.74 mg cm^{-2}. The reference and counter electrodes used for all electrochemical tests were a Hg/HgO electrode and graphite rod, respectively. For all experiments, a 0.1 M KOH solution was used as the electrolyte and purged using oxygen before use. All linear sweep voltammograms (LSVs) and cyclic voltammograms (CVs) were background subtracted using scans collected with N_2 purged 0.1 M KOH. Potentials *vs.* Hg/HgO were converted to *vs.* RHE using the Nernst equation [see eqn (1)].

$$E_{RHE} = E_{Hg/HgO} + 0.0591 \times pH + E^{\circ}_{Hg/HgO} \quad (1)$$

wherein, $E_{Hg/HgO}$ is the measured potential, and $E^{\circ}_{Hg/HgO}$ is the Hg/HgO electrode potential (0.11 V).

For each carbon, LSVs were collected at rotation rates ranging from 400–2500 rpm at a scan rate of 10 mV s^{-1}. The effective number of electrons transferred was calculated using the RRDE method [eqn (2)] and the Koutecky–Leviche (KL) equation [eqn (3)]. Where J^{-1} is the inverse current density, ${J_k}^{-1}$ is the inverse kinetic current density, and $(B\omega^{1/2})^{-1}$ is the inverse limiting current density, wherein ω is the rotation rate. When the current density is plotted against the inverse square root of the rotation rate, the *y*-intercept is ${J_k}^{-1}$ and B^{-1} is the slope. By taking the reciprocal of the slope, the effective number of electrons transferred can be determined. The equation for the reciprocal of the slope, *B*, is shown in eqn (4). In eqn (4), *n* is the effective number of electrons transferred, *F* is Faraday's constant, C_{O_2} is the concentration of oxygen gas, D_{O_2} is the diffusion coefficient of O_2, and *v* is the kinematic viscosity. The coefficient, 0.2, is used here as the rotation rate is in units of revolutions per minute (rpm).

$$n = 4\frac{I_D}{I_D + \frac{I_R}{N}} \quad (2)$$

$$J^{-1} = {J_k}^{-1} + (B\omega^{1/2})^{-1} \quad (3)$$

$$B = 0.2nF{D_{O_2}}^{2/3}v^{-1/6}C_{O_2} \quad (4)$$

While *n* was calculated using both the RRDE method and KL equation, results from employing the RRDE method are primarily discussed as the KL equation assumes a planar electrode surface, which has been shown to be deleterious in determining the selectivity of porous N-doped carbons with respect to the ORR.[42]

Results and discussion

N-doped carbons were prepared according to a two-step procedure[35,36] using melamine as the nitrogen precursor, sucrose as the carbon precursor, and either the pure components or a mixture of Na_2CO_3 and K_2CO_3 for pore generation. In the first step, melamine (80 mass%) and sucrose were semi-carbonized at 410 °C for 2.5 h to prepare an N-doped carbon foam precursor. The resulting foam was then mixed with Na_2CO_3, K_2CO_3, or a mixture of the two alkali carbonate salts. The carbon foam-carbonate mixture was heated to 1000 °C for 60 min at a ramp rate of 3 °C min^{-1} under an argon atmosphere at 150 sccm to induce chemical activation for pore generation. A melamine to sucrose ratio of 80 : 20 was selected, as previous results[36] indicated that activation with Na_2CO_3 or K_2CO_3 would lead to a greater proportion of the total N-content attributable to pyridinic N, which has been reported as selective for the 4-electron pathway of the ORR.[9,12,18] In total, five different N-doped porous carbons were prepared at different mole fractions of Na_2CO_3 to K_2CO_3, designated as 0Na, 25Na, 50Na, 75Na, and 100Na, wherein the numerical value is the mole fraction of Na_2CO_3 in the activating mixture.

During activation, the porosity of the porous carbons was enabled by the decomposition of the alkali carbonates *via* the mechanism shown below, wherein M stands for the alkali cation [eqn (5)–(7)]. Evidence of this mechanism of pore formation is provided in the literature from extensive evolved gas analysis studies with a quadrupole mass spectrometer and X-ray diffraction studies.[36,43–46] In the first step [eqn (5)], upon heating the carbon foam-carbonate mixture to several hundred degrees, the alkali carbonate decomposes into an alkali cyanate (MOCN), which further decomposes to an alkali cyanide (MCN) at ~600 °C.[36,43,46] Depending on the identity of the alkali cation, the onset temperature of M_2CO_3 decomposition varies.[36] Specifically, when the carbon foam precursor is prepared with 80 mass% melamine, K_2CO_3 begins to revert to MOCN at as low as 375 °C, while such decomposition does not begin to occur for Na_2CO_3 until 525 °C.[36] Given N is present in excess in the carbon foam, an abundant amount of these alkali cyanides form. At these elevated temperatures, the alkali cyanides melt, and the

physical properties of the carbon are known to predominantly arise from interactions with the molten salt (*i.e.*, molten salt porogenesis). Given the final synthetic temperature of 1000 °C is in excess of the melting points of KCN and NaCN by at least 400 °C, a molten salt is formed and maintained throughout the activation process. Thus, the porous structure is determined by the alkali carbonate(s) employed and occurs *via* molten salt templating.

$$M_2CO_3 + 2(-CN) \rightarrow 2MOCN + CO \quad (5)$$

$$M_2CO_3 + 2(-CN) \rightarrow MOCN + MCN + CO_2 \quad (6)$$

$$MOCN + (-C) \rightarrow MCN + CO \quad (7)$$

The alkali carbonates Na_2CO_3 and K_2CO_3 were selected for activation rather than other carbonates, such as Li_2CO_3, because previous work[36] showed that these two alkali carbonates resulted in N-doped carbons with a large proportion of pyridinic N and pore volumes composed largely of mesopores. As pyridinic N and mesopores have been attributed to improved electrocatalytic ORR performance and selectivity *via* the introduction of active sites and enabling improved mass transport, respectively,[12,18,23,24,27,47,48] this synthetic method was uniquely posited for the preparation of N-doped carbons as ORR electrocatalysts.

As aforementioned, instead of inducing porosity with only pure Na_2CO_3 or K_2CO_3, mixtures of the two carbonates were employed because the identity of the alkali cation was found to lead to different porous structures while maintaining N composition.[35] As such, porosity effects were studied independent of N-content, and by changing the mol fraction of each activating agent, differing porosities were realized. Thus, by preparing N-doped carbons using this method, the relationship between porous structure and electrochemical ORR activity and selectivity was studied irrespective of N-content, as it was held essentially constant despite modulating the activating mixture composition. Note that all N-doped carbons were activated at 1000 °C instead of lower temperatures, such as 800 °C, to overcome conductivity losses stemming from excessive N-content[49,50] (*i.e.*, a loss in covalency due to extensive disruption to the network of delocalized electrons of graphitic carbon) that would impede electrocatalytic performance. From past work,[36] preparation at 800 °C led to N-contents of ~23.5 at%, and preliminary testing (not shown) indicated that this N-content was deleterious towards ORR electrocatalysis. Activation at 1000 °C led to reduced N-content *via* the loss of nitrogen as gaseous species such as HCN, N_2, and NCCN.[46]

X-ray photoelectron spectroscopy (XPS) determined the surface composition of the carbons, which is useful for understanding potential active sites for ORR electrocatalysis on the activated carbons and to confirm similar N-content between the samples. From analysis of the XPS spectra, the average N-content for 0–100Na was 1.7 ± 0.5 at% N, with an observed minimum of 1 at% N and a maximum of 2.5 at% N (Fig. 1). In addition, C-content and O-content were also very similar at 92–96 at% and 2.6–3.6 at%, respectively (Fig. 1 and S5). Fig. 1 shows the C, N, and O content for each sample. High resolution N 1s spectra revealed that there was virtually no change in the distribution of N-functionalities with increasing mol fraction of Na_2CO_3 until reaching 100Na (Fig. 1b). Nevertheless, the N-content between samples only varied by ~1.5 at%, within the error of the X-ray photoelectron spectrometer (Fig. 1).[51] In addition, the average N-contents fell within the range of uncertainty of one another (Fig. 1c). At 100Na, there was a clear increase in the intensity of the high-resolution N 1s XPS spectrum at ~398.3 eV, indicating an increase in the abundance of pyridinic N sites (Fig. 1b). This result implies that the larger mol fraction of Na_2CO_3 compared to K_2CO_3 led to slightly greater selection for pyridinic N. This observation is supported by previous work, wherein K^+ was speculated to preferentially form KCN adducts at pyridinic N sites.[52] This selective adduct formation may be disadvantageous for ORR electrocatalysis given C-atoms adjacent to pyridinic N sites have been considered the true active sites for the ORR by many.[11,18,53] However, it should be noted that such low N-contents at 1–2.5 at% make it difficult to make a steadfast conclusion from these data concerning selective tuning of the N composition by varying the mol fraction of Na_2CO_3 and K_2CO_3 because fitting of N-motifs is subject to increased uncertainty at these low concentrations. Thus, overall, the prepared N-doped carbons have nearly identical chemical composition, with activation employing only Na_2CO_3 possibly leading to an increased abundance of pyridinic N sites. All deconvoluted high-resolution XPS spectra can be found in the SI.

Following confirmation of similar N-content among the prepared carbon samples, X-ray diffraction (XRD) determined how varying the mol fraction of Na_2CO_3 in the activating salt mixture (Na_2CO_3, K_2CO_3) affected the structure of the carbons, as differences in crystallinity have been associated with changes in porous structure for carbons[54] and increased stability of carbon materials under alkaline conditions.[55–58] For all samples, two peaks were observed at ~23° and ~44° 2θ, corresponding to the 002 and 101 planes characteristic of turbostratic carbon (Fig. 2a).[59,60] A "tail" was also observed at low 2θ, which is associated with the presence of micropores and a lack of long-range order.[54] The 002 peak was observed because of the stacking of carbon sheets, and the 101 peak was observed because of lateral defects (pores, dopants, *etc.*) in the carbon structure.[60,61] From the XRD patterns, a reduced full width half maximum (FWHM) of the 002 peak was observed with the increasing mol fraction of Na_2CO_3, meaning a more crystalline carbon was obtained. There was also a clear shift to higher 2θ for the 002 peak with increasing Na_2CO_3, which was attributed to an increase in the crystallite size, L_c, associated with the stacking of carbon sheets (Fig. 2a). Fig. 2b highlights the trend between the mol fraction of Na_2CO_3 and d_{002} and L_c, wherein d_{002} decreases with increasing mol fraction of Na_2CO_3 and L_c increases. A larger L_c means more stacked sheets are present, likely because of reduced *d*-spacing *via* increased van der Waals interactions between sheets. This reduced *d*-spacing could limit mass transport of reactants during the ORR, limiting electrocatalytic performance. Additionally, the larger L_c corresponding to increased *X*Na means there are an increased number of edge

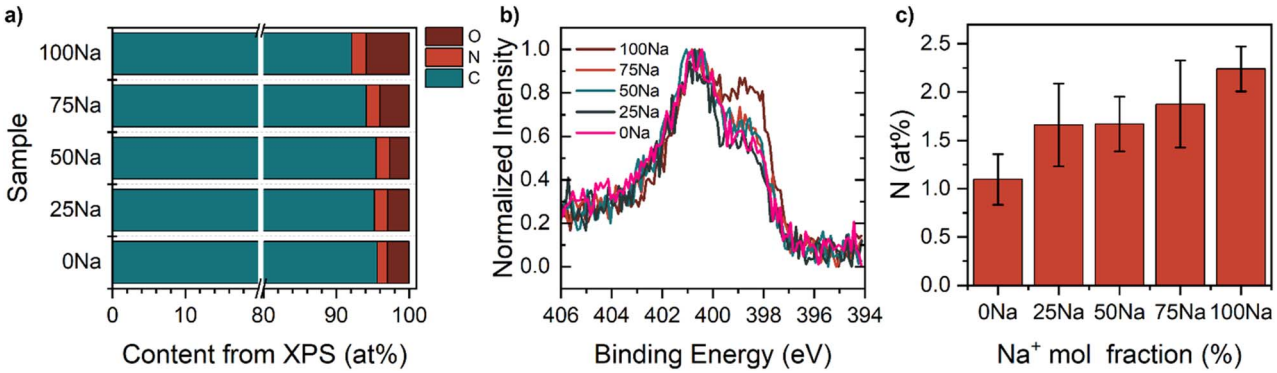

Fig. 1 Chemical composition of the N-doped carbons. (a) Composition for all prepared carbons as determined by XPS. (b) Normalized high-resolution N 1s XPS spectra for all prepared carbons. (c) Average N-content and standard deviation of each activated carbon.

sites exposed to the electrolyte, which have been linked to material degradation under alkaline environments.[55] Thus, employing Na_2CO_3 as an activator could be detrimental to ORR performance and stability owing to the effects of this synthetic handle on the structure of the final activated carbon.

As aforementioned, the structure of the prepared N-doped carbons is delegated by the alkali cyanides that form the molten salt for pore generation. These alkali cyanides act as structure-guiding agents, retaining the local structure of their crystal forms, while having the physical properties of a liquid.[62,63] Essentially, the molten phase of these templates has ordering capabilities while being a liquid consisting of salt ions at high temperatures,[64] hence the term 'ionothermal liquid,' which can be used in place of 'molten salt.'[65] During synthesis, the cations and anions of the molten phase interact with the carbon precursor to generate a more ordered, porous N-doped carbon, as compared to porous carbons prepared *via* chemical etching, to give one example.[36,46] The templating occurs *via* interaction of the cation and anion with the carbon precursor such that charge balance is achieved, wherein the generated pores are dependent on the ion pair and the formation of salt clusters.[66] As such, the larger cation, K^+ *vs.* Na^+, will likely lead to more open structures being obtained. Herein, this appears to be the case—as the mol fraction of Na^+ activator decreased (K^+ activator, K_2CO_3, increased), larger *d*-spacings were observed along the 002 plane indicative of a more open structure.

Considering the cations involved in molten salt templating will affect the final carbon structure *via* their size but also through ionic interactions, the charge density of each activating mixture employed to prepare the carbons 0–100Na was also evaluated with respect to the fringe parameters discussed above (d_{002}, L_c). As shown in Fig. 2, the *d*-spacing along the 002 plane decreased with increasing mol fraction of Na^+, which corresponds to increasing charge density (Fig. S33). Then, L_c increased with increasing mol fraction of Na^+, also corresponding to an increase in charge density (Fig. S34). Thus, increased charge density within the molten salt phase led to templated porous N-doped carbons with more restricted space between stacked carbon sheets and increased crystallinity. The smaller d_{002} with increasing mol fraction Na^+ (increased charge density in activation mixture), could be disadvantageous towards ORR electrocatalysis *via* limiting mass transport of O_2 and reaction intermediates.

The d_{101}, corresponding to in-plane spacing, was similar for all *X*Na at ~4.1 Å (Fig. S6), indicating that the interplanar spacings between the 101 planes were fairly consistent between

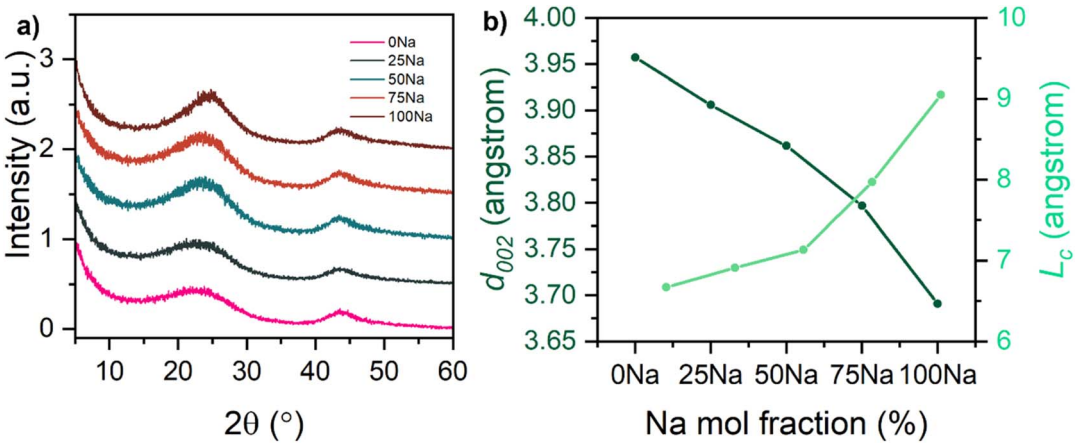

Fig. 2 (Semi)crystallinity of the activated N-doped carbons. (a) XRD patterns, (b) d_{002} and L_c as a function of Na^+ mol fraction.

the N-doped carbons prepared with differing activating mixtures. This observation likely means that the degree of N-doping was similar among 0Na–100Na along the 101 plane as differences in the prevalence of defects, such as dopants, would have likely led to larger deviations in d_{101} values. On the other hand, L_a varied from 29.5–33.5 Å, with larger L_a corresponding to the N-doped carbons prepared with an Na^+ poor (K^+ rich) mixture of the alkali carbonates (Fig. S6). This trend indicates that the average width of a graphitic carbon sheet increased with the increasing K^+ mole fraction (decreasing Na^+) in the activating mixture, which corresponds to a decrease in the charge density of the molten phase during templating. Essentially, decreased charge density during molten salt templating likely led to reduced interaction with the carbon matrix and reduced incurred defects with regard to individual carbon sheets, hence the observed increase in L_a indicative of larger, undisturbed graphitic-like sheets.

In summary, an increased charge density corresponding to an increased Na^+ mol fraction in the activating mixture led to a decrease in the spacing between stacked carbon sheets (d_{002}) and an increased number of stacked carbon sheets along the 002 plane. However, this increased charge density had little effect on the lateral spacing (d_{101}) and was deleterious towards maintaining high order for a given carbon sheet, resulting in decreased sheet width as determined by a decrease in L_a. Thus, while an increase in Na_2CO_3 mol fraction led to increased crystallinity along the 002 plane, it led to smaller d_{002} and less continuous sheets of graphitic carbon. This result indicated that a more K_2CO_3 rich activating mixture may be preferable for the ORR instead, as the corresponding larger d_{002} could enable improved mass transport for the ORR *via* increased accessibility and the increased L_a corresponding to wider carbon sheets could imply less carbon oxidation under alkaline conditions *via* a reduction in edge sites exposed to the electrolyte.[55]

Beyond XRD, Raman spectroscopy was employed to determine the extent of in-plane defects with the changing mol fraction of Na^+ activator, Na_2CO_3, in the activating mixture implemented for pore generation. Raman spectra were collected from 500 to 3500 cm^{-1} using a 514 nm laser as the excitation source. Each spectrum was fit with six bands at approximately 1250, 1350, 1510, 1600, 2700, and 2900 cm^{-1} corresponding to the D4, D, D3, G, 2D, and G + D bands (Fig. S7).[37–41] The D band at 1350 cm^{-1} is observed because of defects within the carbon structure. The D4 band at ~1250 cm^{-1} and D3 band at ~1500 cm^{-1} are attributed to amorphous character and vibrations associated with the presence of heteroatoms and other defects.[37,38] The G-band at ~1580 cm^{-1} is associated with the stretching mode of sp^2 bonded carbon. Then, the bands at higher wavenumber, 2D and G + D, are overtone bands corresponding to the major D (1350 cm^{-1}) and G (~1580 cm^{-1}) bands, which represent higher vibrational energy transitions that are a multiple of the fundamentally observed frequencies (D and G bands).[39–41] Following the fitting of the Raman spectra, the D and G bands were integrated to determine their intensities and to calculate the I_D to I_G ratio. As shown in Fig. S9, the I_D/I_G decreased with increasing Na^+ mol fraction (decreasing K^+ mol fraction) from 2.9 to 1.4, levelling off at 75% Na^+. Given XPS results indicated similar N-content amongst the prepared carbon samples (Fig. 1 and S5), this difference in I_D/I_G ratio could only arise from differences in structure and porosity, leading to in-plane defects induced by varying the composition of the activating mixture. The observed decrease in I_D/I_G indicates that a Na^+ poor (K^+ rich) activating mixture results in a greater level of defects and, as a result, a decreased degree of graphitization. This observation aligns with XRD results, which indicated decreased crystallinity for carbons prepared with a K^+-rich reaction mixture and increased crystallinity when the mixture was rich in Na^+. In addition, L_a determined from Raman results decreased with increasing Na^+ mol fraction (decreasing K^+ mol fraction), once again, matching with results from XRD. An abundance of K^+, as compared to Na^+, in the activating mixture likely led to an increased number of defects but larger L_a owing to the differing charge densities of the *in situ* formed molten salt templates at elevated temperature. The K^+ rich molten salts were less charge dense, likely leading to differing charge networks that interacted with the carbon at 1000 °C and upon cooling, such that more open structures but increased carbon sheet widths were realized as compared to those rich in Na^+. Thus, from XRD and Raman spectroscopy, an activating mixture poor in Na^+ (rich in K^+), will result in a more defective and open structure with individual carbon sheets exhibiting increased order (larger carbon sheet widths).

Scanning electron microscopy (SEM) images showcased morphological changes of the activated carbons as the mol fraction of the activating mixture was varied. Specifically, larger defects were observed with decreasing Na^+ mol fraction (increasing K^+ mol fraction). These larger defects could positively influence electrocatalytic performance by improving mass transport to active sites within small pores. As shown in Fig. S10, all of the activated carbons consisted of micron-scale particles ranging from 10–40 μm in diameter. For the carbons activated with both K_2CO_3 and Na_2CO_3 (25Na, 50Na, and 75Na), additional particulates were formed on the surface of these micron-scale particles, ranging from a few microns in diameter to hundreds of nanometers. For those carbons activated with either pure K_2CO_3 or Na_2CO_3, only the 10–40 μm particles were observed. In addition, as shown in Fig. S10, at the micron scale, surface defects are observed for 0Na–75Na but not for 100Na at the maximum achievable magnifications for imaging. This observation indicates that increasing the mol fraction of Na^+ led to reduced surface defects at the micron scale, meaning more K^+ led to a more defective surface. This increased presence of defects with respect to K^+ could be the result of its increased size and decreased charge density as compared to Na^+ during the templating process. The defects observed from these SEM images likely represent macropores (>50 nm in diameter), which could enable improved transport of O_2 to smaller pores for enhanced electrocatalytic ORR performance. STEM images were attempted of the 50Na sample to obtain more high-resolution images to observe these features, however, high-quality images could not be obtained at the nanometer scale due to the amorphous character of the carbon (Fig. S35). Nevertheless, the presence of macropores was confirmed *via* N_2 porosimetry,

which is discussed in more detail below (Fig. 3). Thus, the increased presence of defects that occur by employing an increased K^+ activator in the activating mixture is likely beneficial towards the ORR *via* the generation of hierarchical porous networks that afford high accessibility of electroactive species to active sites within small pores.

Because of the influence of surface area and pore size on electrocatalytic performance and, specifically, mass transport for the ORR, nitrogen isotherms were collected at 77 K for each N-doped carbon sample to determine their BET SA and extract pore size distribution information using kernels derived from NLDFT on carbon. The isotherms were mixed type I and IV isotherms with H4 hysteresis, indicating that the carbons consisted of both micro- and mesopores (Fig. S11). From the isotherms, it was clear that N_2 uptake decreased with the increasing mol fraction of Na^+ activator, meaning that a greater mol fraction of Na^+ led to lower BET SAs. This observation/finding was confirmed by multi-point BET analysis, wherein point selection satisfied the Rouquerol criteria (positive *C*-value, the p/p_0 value corresponding to monolayer coverage fell within the BET analysis range, *etc.*) (Fig. S12).[67] As shown in Fig. 3a, the BET SA decreased with increasing mol fraction of Na^+ from 1202 to 773 $m^2\ g^{-1}$. Pore size distributions showed that absolute micropore volume decreased with increasing mol fraction of Na^+, as observed with BET SA (Fig. 3a). The absolute mesopore volume ranged from 0.15–0.24 $cm^3\ g^{-1}$, wherein the maximum mesopore volume was observed for the 50Na carbon prepared with an equimolar activating mixture of Na_2CO_3 and K_2CO_3. As such, the absolute mesopore volume increased with increasing charge density of the activating mixture until the activating mixture consisted of 75% Na_2CO_3. For 75Na and 100Na, the absolute mesopore volumes were essentially the same at ~0.18 $cm^3\ g^{-1}$. Mesopore formation may have been hindered because of pore collapse and deformation. This pore collapse and deformation likely arose *via* the loss of N as HCN, N_2, and NCCN, as the precursor contained approximately 45 at% N while the activated carbons had 1.7 ± 0.5 at% N at the surface.[46] However, similar N-loss attributable to pore collapse is expected between the samples because the carbons were prepared from the same precursor and had consistent final N-content. As such, this difference in mesoporosity likely resulted from molten salt templating effects. Specifically, the incorporation of different cations has been shown to alter pure molten salts, indicating that a mixed alkali-cation molten phase could give rise to drastically different charge networks for structure guidance and pore formation.[68,69] Additionally, at increased temperature, the arrangement of the molten phase has been shown to vary, leading to the disruption or loss of charge networks,[68] which could influence porogenesis upon cooling and, ultimately, O_2 transport through porous carbon for electrocatalysis.

Nevertheless, given the inclusion of Na_2CO_3 in the activating mixture led to a limited volume of micropores, this sample set enables clarification of the impact of micropores on ORR electrocatalysis. When the micropore volume of the carbon is subdivided into two groups: 1–2 nm pore volume and <1 nm pore volume, only the pore volume for pores <1 nm decreased with increasing mol fraction of Na^+ activator. This observation indicates that tunability *via* the mol fraction of Na^+ arises from modulation of very small pores. This effect of Na^+ mol fraction on the smallest pore sizes is supported by the relative pore size distribution shown in Fig. 3b, wherein the proportion of pore volume associated with <1 nm micropores decreased from 56 to 32% with increasing mol fraction of Na^+ while that for 1–2 nm pore volumes was consistent between samples. Thus, the mol fraction of Na^+ affects the volume of micropores <1 nm such that the BET SA decreases with increasing mol fraction of Na^+. Such reduced micropore volume and BET SA could hinder mass transport of O_2 for ORR electrocatalysis.

In addition to N_2 porosimetry, CO_2 porosimetry was performed to further characterize microporosity, as microporosity has been attributed to improved performance *via* trapping of O_2 molecules and providing an increased number of accessible active sites for ORR electrocatalysis.[23,52] The CO_2 isotherms were collected at 0 °C and kernels derived from NLDFT on carbon were applied to determine pore size distributions. As shown in Fig. S14, CO_2 adsorption was very similar amongst the activated N-doped carbons. The cumulative pore volume ranged from ~0.03 to 0.05 $cm^3\ g^{-1}$, and the pore size distributions were nearly identical between samples with pore widths of less than 0.4 nm, from 0.4 to 0.6 nm, and from 0.7 to 1.4 nm (Fig. S14).

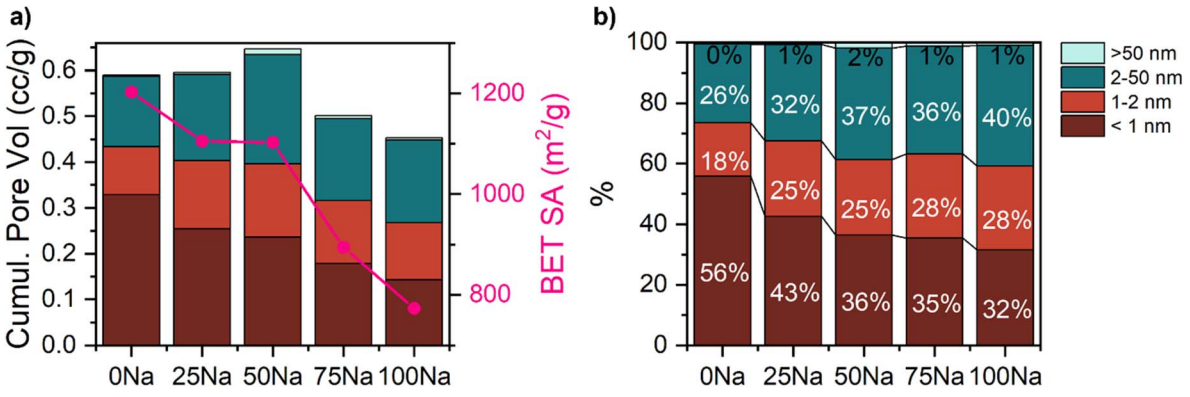

Fig. 3 Surface area and porous structure of activated N-doped carbons. (a) Cumulative pore volume, pore size distribution, and BET surface area, (b) relative pore size distribution.

Deviations in pore volume were only observable for volumes associated with pores from 0.6 to 1.4 nm in diameter. Such a difference in pore volume associated with ~1 nm diameter was also observed from N_2 porosimetry measurements, which can probe pore widths as small as ~0.7 nm in diameter (Fig. 3).[67] Thus, while the mole fraction of Na^+ does not appear to lead to extensive alterations to ultramicroporosity volume (<0.7 nm), there is a clear effect on pore volumes within the micropore regime (0.7 to 1.4 nm).

When the BET SA and N_2 pore size distribution data were compared with structural data, strong correlations with fringe parameters determined from XRD patterns, especially the *d*-spacing of the 002 plane, were observed. Both the BET SA and small micropore volume (<1 nm) correlated positively with d_{002}, while other variables (1–2 nm, 2–50 nm, > 50 nm, and total pore volume) reached their maximum at 50Na (Fig. S34). Given d_{002} depends on the mol fraction of Na^+ activator as discussed above, the correlations with BET SA and pore volume < 1 nm indicate that the mol fraction of Na^+ has a direct effect on the generated porous structure. Specifically, increased Na^+ mol fraction leads to more ordered surfaces as indicated by the decrease in d_{002} and reduced FWMH of the d_{002} peak from XRD (Fig. 2). As such, the Na^+ activator yields more ordered crystal growth for porogenesis *via* molten-salt-templating, which entails fewer defects, explaining the reduced micropore volume of the carbons prepared with Na^+-rich activating mixtures. This trend also correlates with the charge density of the molten phase, which increased with increasing mol fraction of Na^+ activator. Thus, a more charge-dense molten salt led to more ordered carbons at the expense of microporosity. Thus, the K^+-rich activating mixtures (Na^+-poor) with reduced charge density generated more open porous structures with increased microporosity, which could enable improved mass transport during the ORR to boost performance.

Following analysis of physicochemical properties, the activated N-doped carbons were evaluated as ORR electrocatalysts using a RRDE setup. Overall, the prepared carbons demonstrated similar values for E_{onset} (0.719–0.792 ± 0.004–0.015 V *vs.* RHE), which only varied significantly when comparing the carbons activated with the pure components of the activating mixture (Fig. 4). On the other hand, values of $E_{1/2}$ did vary between the porous N-doped carbons, wherein $E_{1/2}$ decreased with increasing Na^+ mol fraction in the activating mixture from 0.691 to 0.557 V *vs.* RHE. However, there was not an obvious difference in selectivity, *n*, between the carbons with the exception of the 100Na sample, considering the uncertainty in *n* for 0–75Na (there was observed overlap of the standard deviation for *n* between these carbons). At 0.7 V *vs.* RHE, $n = \sim 3.9$ for 0–75Na, while $n = 3.5$ for 100Na (Fig. 4d). Nevertheless, for all the carbons, *n* decreased with decreasing potential, stabilizing around 3.2–3.6 at potentials below 0.5 V *vs.* RHE (Fig. S26).

With regard to E_{onset}, the similarity in this value between the carbons (0.719–0.792 ± 0.004–0.015 V *vs.* RHE), indicated that E_{onset} was primarily tuned by the chemical composition, the N-content and N-motif distribution of the carbons. As aforementioned, N-sites function as inducers of active sites *via* a partial positive charge on C atoms.[18,23] Given the carbons all have, statistically, the same N-content, similar E_{onset} is unsurprising. However, despite this predominant effect of N-content, a minute effect from BET SA and porosity is observed. As shown in Fig. 4b, c and f, 0Na and 100Na have different E_{onset} at 0.782 ± 0.004 and 0.719 ± 0.006 V, respectively. This difference arises from differences in their BET SA and porous structure, as their N-, O-, and C-content did not differ drastically from each other (Fig. S5). Of the carbons studied, 0Na had the largest d_{002}, BET SA, and pore volume associated with pores < 1 nm in diameter, while 100Na had the smallest associated values (Fig. 2 and 3). The increased surface area and more open structure of 0Na, as indicated by its larger d_{002}, BET SA, and small micropore volume, likely contributed to improved E_{onset} *via* increased access to N-sites for electrocatalysis. Interestingly, 75Na had a more similar E_{onset} to 0Na than 100Na (Fig. 4f). Given the standard deviation of E_{onset} for 75Na falls within the spread of E_{onset} for other carbons prepared with K^+ in addition to Na^+, these results imply that there may be threshold pore volumes and BET SA that correlate with increased access to N-sites such that E_{onset} becomes increasingly positive. For the studied sample set, these threshold values appear to be a pore volume associated with <1 nm pores of greater than 0.15 $cm^3\ g^{-1}$ and a BET SA of greater than 770 $m^2\ g^{-1}$ (Fig. 3). Thus, the structure and porosity of N-doped carbons can influence kinetic parameters such as E_{onset} by modulating the number of exposed active sites to the electrolyte. Additionally, the positive correlation between E_{onset} and small micropore volume, as shown in Fig. 5a, indicates that these small pores are beneficial towards ORR electrocatalysis and likely contain the catalytic centers for electrocatalysis.

Increased variability was observed with respect to differences in $E_{1/2}$ between the N-doped carbons. Overall, the value of $E_{1/2}$ increased with decreasing mol fraction of Na^+ (increasing mol fraction of K^+) employed for pore generation, with no overlap in the standard deviation of $E_{1/2}$ values further supporting this observed trend, with the exception of 50Na and 75Na, which had nearly identical relative pore size distribution (Fig. 4c and e). Given $E_{1/2}$ resides in the mixed control region of the LSV, it is influenced by both kinetics and mass transport limitations of the carbon materials. The similarity in E_{onset} indicated that kinetics are quite similar between the carbons because of similarities in chemical composition, implying that changes in $E_{1/2}$ are primarily tuned by differences in mass transport that arise from differences in textural properties. Specifically, $E_{1/2}$ was most positive at 0.691 ± 0.004 V *vs.* RHE for 0Na with the largest BET SA, micropore volume, largest d_{002}, and I_D/I_G ratio (Fig. 2, 3, and S9). The $E_{1/2}$ decreased with increased Na^+ mol fraction, which corresponded to a decrease in BET SA, micropore volume, d_{002}, and I_D/I_G ratio: an increase in Na^+ mol fraction led to reduced BET SA, micropore volume, and 'openness' between carbon sheets such that mass transport of O_2 is increasingly limited. As discussed above, this decrease in hierarchical porous structure originates from an increase in charge density of the molten salt phase during templating at 1000 °C. Thus, using K_2CO_3 alone for molten salt templating appears most beneficial for imparting the optimal porous, (semi)

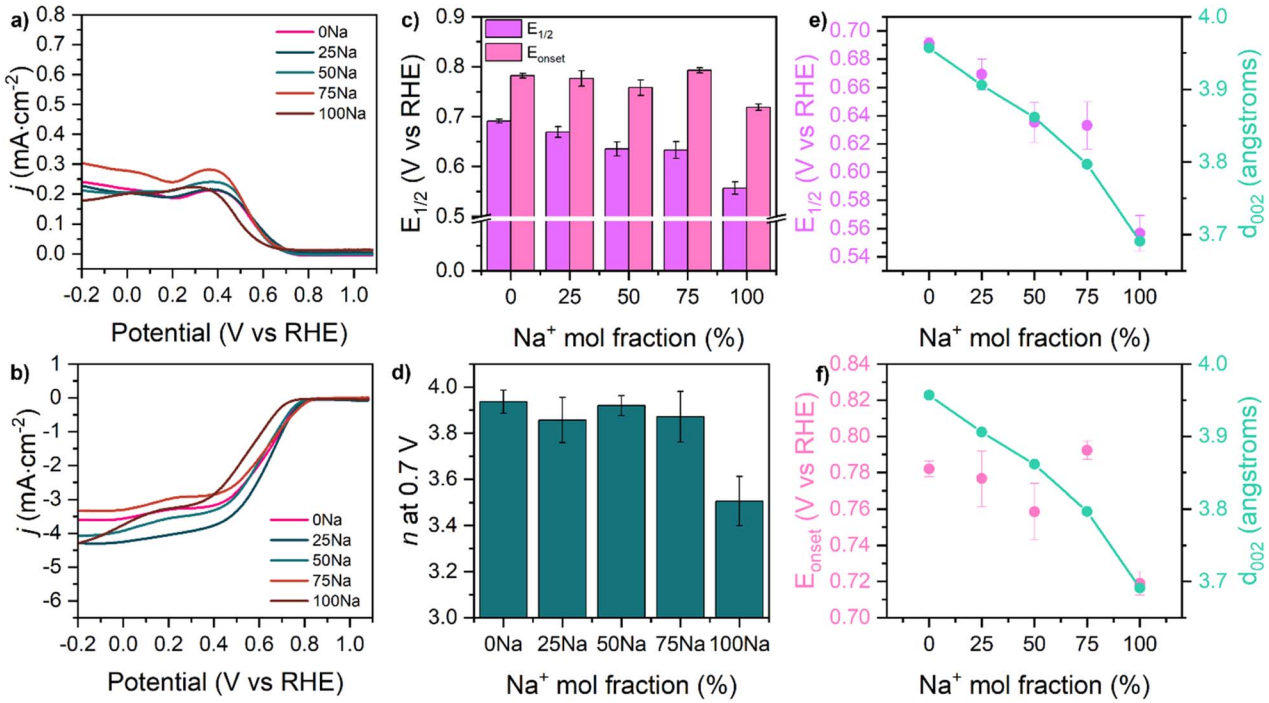

Fig. 4 ORR electrocatalytic performance of the activated N-doped carbons. (a) Ring current response at 1.5 V *vs.* RHE, (b) LSV, (c) bar chart of $E_{1/2}$ and E_{onset}, (d) n, (e) correlation of E_{onset} and d_{002} with mol fraction Na^+, (f) correlation of $E_{1/2}$ and d_{002} with mol fraction Na^+.

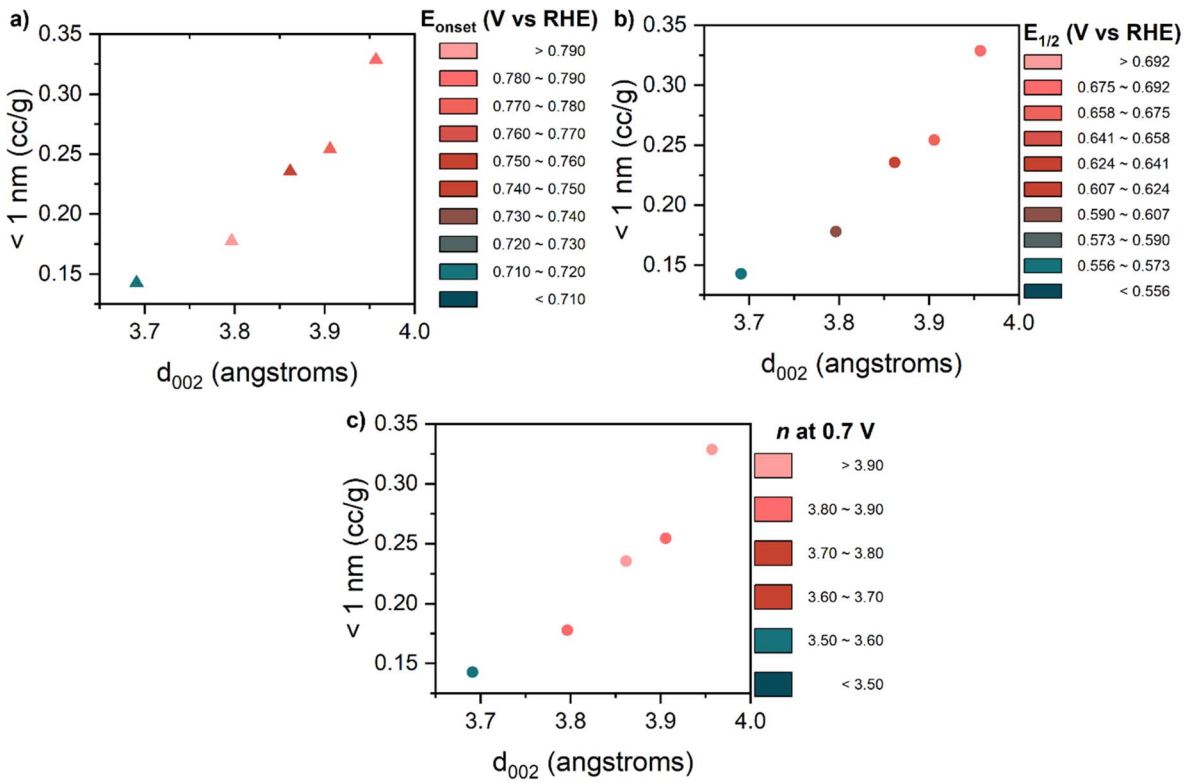

Fig. 5 Correlations of d_{002}, micropore volume (<1 nm) determined from N_2 porosimetry at 77 K with (a) E_{onset}, (b) $E_{1/2}$, and (c) n at 0.7 V *vs.* RHE.

crystalline, and defective structure for this sample set with respect to ORR electrocatalysis.

While the activator(s) employed and the fractions of them used for synthesis had a clear effect on $E_{1/2}$, there was no clear influence on selectivity, n, beyond there being a clear difference between 100Na and the 0–75Na samples (Fig. 4). At 0.7 V *vs.* RHE, for 0–75Na, n was ~3.8–3.9, indicative of high selectivity for the 4e$^-$ pathway of the ORR. On the other hand, 100Na had an n of 3.5 ± 0.1, implying that the 2e$^-$ pathway is occurring alongside the 4e$^-$ pathway to a greater extent than for the carbons activated with a proportion of the K^+ activator. Given the similar chemical composition between the 0–75Na carbons and 100Na (Fig. S5), this difference arises from their differences in structural and textural properties. With regard to structural properties, d_{002}, indicative of the spacing between stacked carbon sheets, was reduced for 100Na as compared to 0–75Na (Fig. 2). The larger d_{002} of the 0–75Na samples, from ~3.95 to 3.80 Å, respectively, indicates a more open structure for O_2 transport through the carbon material, as compared to 100Na with a d_{002} of 3.69 Å. Despite the mere ~0.10–0.25 Å difference in d_{002}, this difference in n likely occurs owing to the kinetic diameter of O_2 at ~3.5 Å, as O_2 would experience more limited transport to active sites through the more confined space between carbon sheets for 100Na as compared to 0–75Na. In addition, as seen from the Raman spectra in Fig. S7, the extent of defects dramatically decreased from 0 to 100Na, wherein the peak intensity of the G-band surpassed that of the D-band. This result indicates that, when no K^+ is present for activation, a less defective doped carbon is produced, leading to a more restricted structure, preventing transport to active sites. This concept is supported by the reduced BET SA and pore volume observed for 100Na as compared to the 0–75Na samples (Fig. 3). The smaller BET SA and pore volume of 100Na likely led to restricted access of O_2 to smaller pores, as probed by CO_2 at 0 °C (Fig. S14). Despite 100Na having nearly identical CO_2 accessible pore volume to the 0–75Na carbons at 0 °C, this volume was less accessible owing to its reduced volume associated with larger pores, as probed by N_2 at 77 K (Fig. 3). Thus, the reduced selectivity, n, at 0.7 V *vs.* RHE for 100Na *vs.* 0–75Na is likely a result of a portion of active sites being essentially blocked from participation in the ORR and a lack of an interconnected pore network for the facilitation of O_2 transport.

However, as the applied potential decreased, the selectivity, n, was no longer different between 100Na and 0–75Na (Fig. S26). This result implies that with decreasing potential, there is increased driving force for the ORR to proceed *via* the 4e$^-$ pathway. Further analysis of the LSVs indicates that this apparent favorability for the 4e$^-$ pathway for 100Na is actually the result of indirect 4e$^-$ transfer rather than the direct 4e$^-$ pathway. Specifically, as shown in Fig. 4b, for 100Na, a pseudo-limiting current density is obtained at ~0.4 V *vs.* RHE, only for the current density to decrease further and reach a new limiting current density. This "two-wave" behavior is indicative of a 2-step 2-electron reduction reaction. Specifically, O_2 is reduced to HO_2^- *via* 2-electrons followed by 2-electron reduction of HO_2^- to hydroxide ions.[33,70] This 2-step reduction process can occur as a result of tortuous networks within the N-doped carbon. Essentially, due to these tortuous networks, HO_2^- molecules have a longer lifetime at the working electrode, leading to further reduction to hydroxide ions *via* 2-electrons rather than being transported to and detected at the Pt ring of the RRDE. Thus, this 'two-wave' behavior can lead to an observed selectivity, n, nearing 4 (Fig. 4b and S26). As discussed, this 4-electron transfer consists of two discrete steps and not the direct 4-electron pathway of the ORR. Thus, when this behavior is observed, the extent to which the direct 4-electron pathway occurs may be inflated, especially at more negative potentials.

Upon further observation of the LSV shapes of the activated carbons, this behavior is also clearly visible for 75Na and 50Na, although to a lesser extent. Thus, for 75Na and 50Na it is likely that the indirect 4e$^-$ pathway is being catalyzed in addition to direct 4e$^-$ transfer, which is supported by the decrease in n from ~3.8 at 0.7 V (*vs.* RHE) to less than 3.8 with decreasing potential. From Fig. S26, this observation appears likely as there is a more dramatic change in n with decreasing potential for 50–100Na than 0Na and 25 Na. This difference in selectivity between the N-doped, porous carbons trends with the relative micropore volume for pores < 1 nm, as determined from N_2 porosimetry at 77 K. Specifically, 0Na and 25Na consisted of 56 and 43% of pores < 1 nm in diameter, while 50Na, 75Na, and 100Na were at 36, 35, and 32%, respectively. Thus, the tuning of micropores *via* modulation of the activating mixture resulted in less porous carbons, such that tortuous porous networks contributed to indirect 4e$^-$ transfer *via* a 2-step 2-electron reduction rather than direct 4e$^-$ transfer. Specifically, a decreased mol fraction of Na^+ (increased K^+) led to increased microporosity such that the direct 4e$^-$ pathway was selectively achieved. This hypothesis is further supported by the double layer capacitance (C_{dl}), which acts as a proxy for electrochemically active surface area. As shown in Fig. S29 and S30, C_{dl} is largest for 0Na and 25Na, matching with N_2 porosimetry results that indicated these samples had the largest and most accessible surface for the ORR.

In addition to selectivity, variability was also observed between samples concerning limiting current (Fig. 4b). An increased limiting current is often associated with increased electrochemically active surface area or surface area in general, as limiting current is reached when the reaction rate is entirely controlled by mass transfer and not kinetics. However, this correlation is not always observed, as for the carbons studied herein. This trend between limiting current and surface area is likely not observed for multiple reasons: (1) variability in surface roughness and electrode geometry leading to differing thicknesses in the diffusion layer at the disk of the RRDE that impacts the current response in the mass-transfer controlled region,[71] (2) those carbons (50–100Na) undergoing an additional 2-electron reduction step, as compared to 0 and 25Na, indicative of additional kinetic effects and not pure mass transfer control, which makes direct comparison of the current response past 0.4 V *vs.* RHE challenging, (3) limiting current densities falling within a standard deviation of one another as result of similarities in pore size distributions, such as for 0 and 25Na, and the limitations of drop-casting for electrode

preparation.[72] As such, it is difficult to compare samples in terms of limiting current at reduced potentials.

Nevertheless, given the most significant differences in electrochemical performance and selectivity were observed for the two extremes of the sample set, 0Na and 100Na, these two carbons were evaluated for long-term stability. Chronoamperometry was performed for 24 h at an applied potential of 0.4 V *vs.* RHE. In addition, SEM images were taken before and after chronoamperometry to gauge changes to morphology. As shown in Fig. S31, both 0Na and 100Na exhibited a steep decay in signal over the first 3–4 hours of long-term testing. Then, a gradual decay in current density was observed from 4–24 hours. Of the two samples, 100Na demonstrated increased decay, as compared to 0Na, with current density decaying by 25% compared to 20% for 0Na at 3.4 h. Additionally, the current density for 100Na also exhibited increased decay from 3.4 h to 24 h at 33% compared to 0Na at 24%. While these decays in current density are large, the reduced decay in current density of 0Na as compared to 100Na indicates that increased in-plane order and a reduced number of edge sites contribute to improved stability. As discussed above, 0Na with an activation mixture consisting entirely of K_2CO_3 and, as a result, K^+ ions during molten salt templating, had a larger L_a as compared to 100Na prepared with 100% Na_2CO_3 for pore generation. This increased L_a for 0Na *vs.* 100Na was observed with both XRD and Raman spectroscopy (Fig. S6) and corresponded to increased in-plane order and width of graphitic carbon sheets. This increased lateral order led to a reduced number of edge sites, which have been considered as 'hot spots' for carbon oxidation under alkaline conditions.[55] Thus, 0Na demonstrated increased stability compared to 100Na.

While a clear decay in current density was observed for 0Na and 100Na, the comparison of SEM images taken before and after long-term testing showed no obvious changes in morphology on the micron scale (Fig. S32). Thus, current density decay is likely the result of changes to the nanostructure of the N-doped, porous carbons or changes in chemical composition, as has been discussed in past literature.[24,48] Given the similar chemical composition of 0Na and 100Na (Fig. 1), current decay related to surface group transformation was likely similar, as reflected by the ~5% difference in current decay after 3.4 h of long-term testing. However, as discussed above, 100Na possibly underwent further oxidation as compared to 0Na with time because of decreased lateral order prior to ORR electrocatalytic testing. Essentially, the increased number of edge sites of 100Na likely led to increased oxidation and a further disordering of the microstructure, which would lead to even further degradation of the carbon material.

To further gauge material transformation during stability testing, Raman spectroscopy was performed before and after long-term testing (24 h, chronoamperometry) of the 0Na sample on a rotating ring disk electrode (RRDE) (Fig. S33). Following this long-term test, the I_D/I_G ratio decreased from 2.16 to 1.57, indicating a loss in disorder to the carbon electrocatalysts. Given the D peak at 1350 cm^{-1} arises because of defects in the carbon material, this decrease implies that those defects are somehow being lost. A reduction in the level of defects is likely the result of either the loss of N-dopants or the agglomeration of nanometer diameter pores. Thus, although N-doped carbon electrocatalysts are operating under reducing potentials, there is still material degradation occurring.

Conclusions

The effect of structural and textural properties of N-doped porous carbons on their ORR performance independent of N-content was determined. N-doped porous carbons with variable porosity but consistent N-content and nearly identical N-motif distribution were prepared by employing a two-step synthetic method. In the first step, a N-doped carbon foam precursor was prepared using 80 mass% of the N precursor, melamine. In step two, the resulting carbon foam precursor was pyrolyzed in the presence of an activating mixture to generate porosity. The composition of this activating mixture consisted of Na_2CO_3 and/or K_2CO_3. By varying the makeup of the activating mixture, different structural and textural properties were obtained. Physicochemical characterization (XRD, Raman spectroscopy, N_2 porosimetry, *etc.*) revealed that an Na_2CO_3 poor but K_2CO_3 rich mixture resulted in increased d_{002}, extent of defects, porosity, and BET SA, corresponding to a more open and accessible hierarchical porous structure for improved ORR electrocatalysis. This increase in open, hierarchical porous structure for the promotion of the ORR occurred because the alkali carbonates interacted with the carbon foam precursor, forming alkali cyanides that melted at elevated temperatures, leading to molten salt templating as the pathway of pore formation.[36,46] Because a molten phase rich in K_2CO_3 would lead to increased K^+ content and decreased charge density for molten salt templating, increased surface area and accessible porosity were achieved. Specifically, those N-doped carbons prepared with more K_2CO_3 rich mixtures demonstrated more positive values of $E_{1/2}$ (Fig. 4). Additionally, while the values of E_{onset} and selectivity, n, were similar between all the carbons prepared with some proportion of K_2CO_3 in the activating mixture, there was a difference in these two variables when comparing the N-doped porous carbons prepared with either 100% Na_2CO_3 (100Na) or 0–75% (0–75Na). The difference between the two extremes of the sample set was attributed to the reduced d_{002} and microporosity of 100Na. Specifically, 100Na had a d_{002} of only 3.69 Å, while 0–75Na had d_{002} ranging from 3.80–3.95 Å, making it less accommodating for an O_2 molecule with a kinetic diameter of 3.46 Å. Additionally, 100Na had reduced absolute and relative micropore volumes compared to the samples prepared with an activating mixture with 25–100% K_2CO_3. And, although 100Na and 75Na had fairly similar pore volumes and pore size distributions, the BET SA for 100Na was reduced by ~120 $cm^3\ g^{-1}$ compared to 75Na, indicating that 100Na had a more restricted and less accessible porous structure as compared to other samples. Thus, a reduced E_{onset} and n were observed for 100Na, as compared to the rest of the sample set, because of a more tortuous porous network limiting transport and access to and from active sites. In addition, long-term testing of 0Na and 100Na indicated that 0Na demonstrated improved stability owing to increased lateral order that limited

the number of exposed edge sites for carbon oxidation, as indicated by an increased L_a compared to 100Na. Additionally, a decrease in the I_D/I_G for 0Na before and after long-term testing provided further evidence of material degradation as a result of the loss of dopants and/or pore collapse. Thus, an abundance of micropores (<1 nm), increased BET SA, and heightened lateral order led to improved ORR performance *via* enhanced mass transport to active sites, access to said sites, and by limiting the number of edge sites contributory to carbon degradation. Long-term testing also revealed that carbon degradation occurred, even under reducing potentials, indicating the need for post-ORR characterization in future work to further understand N-doped carbons as electrocatalysts for the oxygen reduction reaction.

Author contributions

Lettie A. Smith: conceptualization, investigation, formal analysis, writing—original draft, writing—review & editing. J. Ehren Eichler: conceptualization, investigation, writing—review & editing. Kenta Kawashima: investigation, writing—review & editing. Hanah Leonard: investigation. Franklin Tang: investigation. Ethan Kang Yang: investigation. Wuilian A. Martinez: investigation. Yasaman Karbalaeemorad: investigation. C. Buddie Mullins: project administration, funding acquisition, writing—review & editing.

Conflicts of interest

There are no conflicts of interest.

Data availability

The data supporting this article have been included as part of the SI.

XPS spectra, Raman spectra, fringe parameters, SEM images, N_2 isotherm data, BET plots, cumulative pore volume and pore size distribution data, CO_2 adsorption data, electrochemical data, and STEM images. See DOI: **https://doi.org/10.1039/d5ta04494d**.

Acknowledgements

The authors thank Omnis Energy and the Grant CHE-2102307 (from the National Science Foundation) for their support of this research, and the MRI Grant 2117623 (from the National Science Foundation) for the acquisition of the VersaProbe 4 scanning XPS instrument integral to this study.

References

1 United Nations, *2023 The Sustainable Development Goals Report Special Edition*, United Nations, 2023, **https://unstats.un.org/sdgs/report/2023/The-Sustainable-Development-Goals-Report-2023.pdf**.

2 J. Wang, H. Wang and Y. Fan, Techno-Economic Challenges of Fuel Cell Commercialization, *Engineering*, 2018, **4**(3), 352–360, DOI: **10.1016/j.eng.2018.05.007**.

3 D. K. Niakolas, M. Daletou, S. G. Neophytides and C. G. Vayenas, Fuel Cells Are a Commercially Viable Alternative for the Production of "Clean" Energy, *Ambio*, 2016, **45**(S1), 32–37, DOI: **10.1007/s13280-015-0731-z**.

4 M. E. Abdelrahman, H. Zhang, G. Wu, X. Li and S. Litster, Half-Cell Electrode Assessments of a Crossover-Tolerant Direct Methanol Fuel Cell with a Platinum Group Metal-Free Cathode, *Electrochim. Acta*, 2022, **416**, 140262, DOI: **10.1016/j.electacta.2022.140262**.

5 F. Samimi and M. R. Rahimpour, Direct Methanol Fuel Cell, in *Methanol*, Elsevier, 2018, pp 381–397, DOI: **10.1016/B978-0-444-63903-5.00014-5**.

6 B. Wu, H. Meng, D. M. Morales, F. Zeng, J. Zhu, B. Wang, M. Risch, Z. J. Xu and T. Petit, Nitrogen-Rich Carbonaceous Materials for Advanced Oxygen Electrocatalysis: Synthesis, Characterization, and Activity of Nitrogen Sites, *Adv. Funct. Mater.*, 2022, **32**(31), 2204137, DOI: **10.1002/adfm.202204137**.

7 A. Kongkanand and M. F. Mathias, The Priority and Challenge of High-Power Performance of Low-Platinum Proton-Exchange Membrane Fuel Cells, *J. Phys. Chem. Lett.*, 2016, **7**(7), 1127–1137, DOI: **10.1021/acs.jpclett.6b00216**.

8 B. Baruah and P. Deb, Performance and Application of Carbon-Based Electrocatalysts in Direct Methanol Fuel Cell, *Mater. Adv.*, 2021, **2**(16), 5344–5364, DOI: **10.1039/D1MA00503K**.

9 R. Ma, G. Lin, Y. Zhou, Q. Liu, T. Zhang, G. Shan, M. Yang and J. Wang, A Review of Oxygen Reduction Mechanisms for Metal-Free Carbon-Based Electrocatalysts, *Npj Comput. Mater.*, 2019, **5**(1), 78, DOI: **10.1038/s41524-019-0210-3**.

10 H. Jiang, J. Gu, X. Zheng, M. Liu, X. Qiu, L. Wang, W. Li, Z. Chen, X. Ji and J. Li, Defect-Rich and Ultrathin N Doped Carbon Nanosheets as Advanced Trifunctional Metal-Free Electrocatalysts for the ORR, OER and HER, *Energy Environ. Sci.*, 2019, **12**(1), 322–333, DOI: **10.1039/C8EE03276A**.

11 G. A. Ferrero, A. B. Fuertes, M. Sevilla and M.-M. Titirici, Efficient Metal-Free N-Doped Mesoporous Carbon Catalysts for ORR by a Template-Free Approach, *Carbon*, 2016, **106**, 179–187, DOI: **10.1016/j.carbon.2016.04.080**.

12 G. A. Ferrero, K. Preuss, A. B. Fuertes, M. Sevilla and M.-M. Titirici, The Influence of Pore Size Distribution on the Oxygen Reduction Reaction Performance in Nitrogen Doped Carbon Microspheres, *J. Mater. Chem. A*, 2016, **4**(7), 2581–2589, DOI: **10.1039/C5TA10063A**.

13 Q. Lv, W. Si, J. He, L. Sun, C. Zhang, N. Wang, Z. Yang, X. Li, X. Wang, W. Deng, Y. Long, C. Huang and Y. Li, Selectively Nitrogen-Doped Carbon Materials as Superior Metal-Free Catalysts for Oxygen Reduction, *Nat. Commun.*, 2018, **9**(1), 3376, DOI: **10.1038/s41467-018-05878-y**.

14 H. Xu, J. Yang, R. Ge, J. Zhang, Y. Li, M. Zhu, L. Dai, S. Li and W. Li, Carbon-Based Bifunctional Electrocatalysts for Oxygen Reduction and Oxygen Evolution Reactions: Optimization Strategies and Mechanistic Analysis, *J. Energy*

Chem., 2022, **71**, 234–265, DOI: 10.1016/j.jechem.2022.03.022.

15 T.-P. Fellinger, F. Hasché, P. Strasser and M. Antonietti, Mesoporous Nitrogen-Doped Carbon for the Electrocatalytic Synthesis of Hydrogen Peroxide, *J. Am. Chem. Soc.*, 2012, **134**(9), 4072–4075, DOI: 10.1021/ja300038p.

16 J. Zhang, G. Zhang, S. Jin, Y. Zhou, Q. Ji, H. Lan, H. Liu and J. Qu, Graphitic N in Nitrogen-Doped Carbon Promotes Hydrogen Peroxide Synthesis from Electrocatalytic Oxygen Reduction, *Carbon*, 2020, **163**, 154–161, DOI: 10.1016/j.carbon.2020.02.084.

17 Y. Zhang, Y. Pang, D. Xia and G. Chai, Regulable Pyrrolic-N-Doped Carbon Materials as an Efficient Electrocatalyst for Selective O_2 Reduction to H_2O_2, *New J. Chem.*, 2022, **46**(30), 14510–14516, DOI: 10.1039/D2NJ02393H.

18 D. Guo, R. Shibuya, C. Akiba, S. Saji, T. Kondo and J. Nakamura, Active Sites of Nitrogen-Doped Carbon Materials for Oxygen Reduction Reaction Clarified Using Model Catalysts, *Science*, 2016, **351**(6271), 361–365, DOI: 10.1126/science.aad0832.

19 H. Shi, Y. Shen, F. He, Y. Li, A. Liu, S. Liu and Y. Zhang, Recent Advances of Doped Carbon as Non-Precious Catalysts for Oxygen Reduction Reaction, *J. Mater. Chem. A*, 2014, **2**(38), 15704–15716, DOI: 10.1039/C4TA02790F.

20 M. Skorupska, A. Ilnicka and J. P. Lukaszewicz, The Effect of Nitrogen Species on the Catalytic Properties of N-Doped Graphene, *Sci. Rep.*, 2021, **11**(1), 23970, DOI: 10.1038/s41598-021-03403-8.

21 D. Wang, J. Hu, J. Wei, X. Liu and H. Hou, Insights into Nitrogen-doped Carbon for Oxygen Reduction: The Role of Graphitic and Pyridinic Nitrogen Species, *ChemPhysChem*, 2023, **24**(10), e202200734, DOI: 10.1002/cphc.202200734.

22 Q. Lai, J. Zheng, Z. Tang, D. Bi, J. Zhao and Y. Liang, Optimal Configuration of N-Doped Carbon Defects in 2D Turbostratic Carbon Nanomesh for Advanced Oxygen Reduction Electrocatalysis, *Angew. Chem.*, 2020, **132**(29), 12097–12104, DOI: 10.1002/ange.202000936.

23 T. J. Bandosz, Revealing the Impact of Small Pores on Oxygen Reduction on Carbon Electrocatalysts: A Journey through Recent Findings, *Carbon*, 2022, **188**, 289–304, DOI: 10.1016/j.carbon.2021.11.071.

24 J. C. Carrillo-Rodríguez, A. M. Garay-Tapia, B. Escobar-Morales, J. Escorcia-García, M. T. Ochoa-Lara, F. J. Rodríguez-Varela and I. L. Alonso-Lemus, Insight into the Performance and Stability of N-Doped Ordered Mesoporous Carbon Hollow Spheres for the ORR: Influence of the Nitrogen Species on Their Catalytic Activity after ADT, *Int. J. Hydrogen Energy*, 2021, **46**(51), 26087–26100, DOI: 10.1016/j.ijhydene.2021.01.047.

25 X. Wang, J. S. Lee, Q. Zhu, J. Liu, Y. Wang and S. Dai, Ammonia-Treated Ordered Mesoporous Carbons as Catalytic Materials for Oxygen Reduction Reaction, *Chem. Mater.*, 2010, **22**(7), 2178–2180, DOI: 10.1021/cm100139d.

26 N. Gavrilov, I. A. Pašti, M. Mitrić, J. Travas-Sejdić, G. Ćirić-Marjanović and S. V. Mentus, Electrocatalysis of Oxygen Reduction Reaction on Polyaniline-Derived Nitrogen-Doped Carbon Nanoparticle Surfaces in Alkaline Media, *J. Power Sources*, 2012, **220**, 306–316, DOI: 10.1016/j.jpowsour.2012.07.119.

27 J. Pampel and T.-P. Fellinger, Opening of Bottleneck Pores for the Improvement of Nitrogen Doped Carbon Electrocatalysts, *Adv. Energy Mater.*, 2016, **6**(8), 1502389, DOI: 10.1002/aenm.201502389.

28 R. Zhou, Y. Zheng, M. Jaroniec and S.-Z. Qiao, Determination of the Electron Transfer Number for the Oxygen Reduction Reaction: From Theory to Experiment, *ACS Catal.*, 2016, **6**(7), 4720–4728, DOI: 10.1021/acscatal.6b01581.

29 D. Eisenberg, P. Prinsen, N. J. Geels, W. Stroek, N. Yan, B. Hua, J.-L. Luo and G. Rothenberg, The Evolution of Hierarchical Porosity in Self-Templated Nitrogen-Doped Carbons and Its Effect on Oxygen Reduction Electrocatalysis, *RSC Adv.*, 2016, **6**(84), 80398–80407, DOI: 10.1039/C6RA16606G.

30 B. Xie, Y. Zhang and R. Zhang, Pure Nitrogen-Doped Graphene Aerogel with Rich Micropores Yields High ORR Performance, *Mater. Sci. Eng. B*, 2019, **242**, 1–5, DOI: 10.1016/j.mseb.2019.02.012.

31 H. Mashhadimoslem, M. Safarzadeh Khosrowshahi, M. Jafari, A. Ghaemi and A. Maleki, Adsorption Equilibrium, Thermodynamic, and Kinetic Study of O_2/N_2/CO_2 on Functionalized Granular Activated Carbon, *ACS Omega*, 2022, **7**(22), 18409–18426, DOI: 10.1021/acsomega.2c00673.

32 K. E. Gubbins and R. D. Walker, The Solubility and Diffusivity of Oxygen in Electrolytic Solutions, *J. Electrochem. Soc.*, 1965, **112**(5), 469, DOI: 10.1149/1.2423575.

33 A. Gabe, R. Ruiz-Rosas, C. González-Gaitán, E. Morallón and D. Cazorla-Amorós, Modeling of Oxygen Reduction Reaction in Porous Carbon Materials in Alkaline Medium. Effect of Microporosity, *J. Power Sources*, 2019, **412**, 451–464, DOI: 10.1016/j.jpowsour.2018.11.075.

34 J. E. Eichler, J. N. Burrow, N. Katyal, G. Henkelman and C. B. Mullins, Modulation of CO_2 Adsorption Thermodynamics and Selectivity in Alkali-Carbonate Activated N-Rich Porous Carbons, *J. Mater. Chem. A*, 2023, **11**(24), 12811–12826, DOI: 10.1039/D2TA09376F.

35 J. E. Eichler, H. Leonard, E. K. Yang, L. A. Smith, S. N. Lauro, J. N. Burrow, R. P. P. L. Ribeiro and C. B. Mullins, Dual-Cation Activation of N-Enriched Porous Carbons Improves Control of CO_2 and N_2 Adsorption Thermodynamics for Selective CO_2 Capture, *Adv. Funct. Mater.*, 2024, 2410171, DOI: 10.1002/adfm.202410171.

36 J. E. Eichler, J. N. Burrow, N. Katyal, G. Henkelman and C. B. Mullins, Modulation of CO_2 Adsorption Thermodynamics and Selectivity in Alkali-Carbonate Activated N-Rich Porous Carbons, *J. Mater. Chem. A*, 2023, **11**(24), 12811–12826, DOI: 10.1039/D2TA09376F.

37 Z. E. Brubaker, J. J. Langford, R. J. Kapsimalis and J. L. Niedziela, Quantitative Analysis of Raman Spectral Parameters for Carbon Fibers: Practical Considerations and Connection to Mechanical Properties, *J. Mater. Sci.*, 2021, **56**(27), 15087–15121, DOI: 10.1007/s10853-021-06225-1.

38 M. Ayiania, E. Weiss-Hortala, M. Smith, J.-S. McEwen and M. Garcia-Perez, Microstructural Analysis of Nitrogen-Doped Char by Raman Spectroscopy: Raman Shift Analysis from First Principles, *Carbon*, 2020, **167**, 559–574, DOI: 10.1016/j.carbon.2020.05.055.

39 A. Maghsoumi, L. Brambilla, C. Castiglioni, K. Müllen and M. Tommasini, Overtone and Combination Features of G and D Peaks in Resonance Raman Spectroscopy of the $C_{78}H_{26}$ Polycyclic Aromatic Hydrocarbon, *J. Raman Spectrosc.*, 2015, **46**(9), 757–764, DOI: 10.1002/jrs.4717.

40 Y. Kawashima and G. Katagiri, Fundamentals, Overtones, and Combinations in the Raman Spectrum of Graphite, *Phys. Rev. B:Condens. Matter Mater. Phys.*, 1995, **52**(14), 10053–10059, DOI: 10.1103/PhysRevB.52.10053.

41 A. C. Ferrari and D. M. Basko, Raman Spectroscopy as a Versatile Tool for Studying the Properties of Graphene, *Nat. Nanotechnol.*, 2013, **8**(4), 235–246, DOI: 10.1038/nnano.2013.46.

42 L. Bouleau, S. Pérez-Rodríguez, J. Quílez-Bermejo, M. T. Izquierdo, F. Xu, V. Fierro and A. Celzard, Best Practices for ORR Performance Evaluation of Metal-Free Porous Carbon Electrocatalysts, *Carbon*, 2022, **189**, 349–361, DOI: 10.1016/j.carbon.2021.12.078.

43 J. V. Guerrera, J. N. Burrow, J. E. Eichler, M. Z. Rahman, M. V. Namireddy, K. A. Friedman, S. S. Coffman, D. C. Calabro and C. B. Mullins, Evaluation of Two Potassium-Based Activation Agents for the Production of Oxygen- and Nitrogen-Doped Porous Carbons, *Energy Fuels*, 2020, **34**(5), 6101–6112, DOI: 10.1021/acs.energyfuels.0c00427.

44 M. Sevilla, N. Díez and A. B. Fuertes, More Sustainable Chemical Activation Strategies for the Production of Porous Carbons, *ChemSusChem*, 2021, **14**(1), 94–117, DOI: 10.1002/cssc.202001838.

45 N. Tsubouchi, M. Nishio and Y. Mochizuki, Role of Nitrogen in Pore Development in Activated Carbon Prepared by Potassium Carbonate Activation of Lignin, *Appl. Surf. Sci.*, 2016, **371**, 301–306, DOI: 10.1016/j.apsusc.2016.02.200.

46 J. E. Eichler, J. N. Burrow, Y. Wang, D. C. Calabro and C. B. Mullins, Unraveling Porogenesis in Nitrogen Rich K+-Activated Carbons, *Carbon*, 2022, **186**, 711–723, DOI: 10.1016/j.carbon.2021.10.041.

47 G. Collins, P. R. Kasturi, R. Karthik, J.-J. Shim, R. Sukanya and C. B. Breslin, Mesoporous Carbon-Based Materials and Their Applications as Non-Precious Metal Electrocatalysts in the Oxygen Reduction Reaction, *Electrochim. Acta*, 2023, **439**, 141678, DOI: 10.1016/j.electacta.2022.141678.

48 T. Xing, Y. Zheng, L. H. Li, B. C. C. Cowie, D. Gunzelmann, S. Z. Qiao, S. Huang and Y. Chen, Observation of Active Sites for Oxygen Reduction Reaction on Nitrogen-Doped Multilayer Graphene, *ACS Nano*, 2014, **8**(7), 6856–6862, DOI: 10.1021/nn501506p.

49 J. D. Wiggins-Camacho and K. J. Stevenson, Effect of Nitrogen Concentration on Capacitance, Density of States, Electronic Conductivity, and Morphology of N-Doped Carbon Nanotube Electrodes, *J. Phys. Chem. C*, 2009, **113**(44), 19082–19090, DOI: 10.1021/jp907160v.

50 Z. R. Ismagilov, A. E. Shalagina, O. Yu. Podyacheva, A. V. Ischenko, L. S. Kibis, A. I. Boronin, Y. A. Chesalov, D. I. Kochubey, A. I. Romanenko, O. B. Anikeeva, T. I. Buryakov and E. N. Tkachev, Structure and Electrical Conductivity of Nitrogen-Doped Carbon Nanofibers, *Carbon*, 2009, **47**(8), 1922–1929, DOI: 10.1016/j.carbon.2009.02.034.

51 C. J. Powell and M. P. Seah, Precision, Accuracy, and Uncertainty in Quantitative Surface Analyses by Auger-Electron Spectroscopy and x-Ray Photoelectron Spectroscopy, *J. Vac. Sci. Technol. Vac. Surf. Films*, 1990, **8**(2), 735–763, DOI: 10.1116/1.576956.

52 L. A. Smith, J. N. Burrow, J. E. Eichler, F. Tang, S. N. Lauro, X. Zhan, J. H. Warner and C. B. Mullins, A Deep Dive Into the Study of Nitrogen-Doped Carbons as Electrocatalysts for the Oxygen Reduction Reaction via Design of Experiments, *Small*, 2025, 2410010, DOI: 10.1002/smll.202410010.

53 K. Takeyasu, M. Furukawa, Y. Shimoyama, S. K. Singh and J. Nakamura, Role of Pyridinic Nitrogen in the Mechanism of the Oxygen Reduction Reaction on Carbon Electrocatalysts, *Angew. Chem., Int. Ed.*, 2021, **60**(10), 5121–5124, DOI: 10.1002/anie.202014323.

54 J. N. Burrow, J. E. Eichler, Y. Wang, D. C. Calabro and C. B. Mullins, N-Rich Porous Carbons with Tunable Affinity for CO_2 Adsorption Achieve Size-Sieving CO_2/N_2 Selectivity in Turbostratic Interlayers, *J. Mater. Chem. A*, 2022, **10**(46), 24649–24661, DOI: 10.1039/D2TA05911H.

55 L. A. Smith, K. Kawashima, R. A. Marquez and C. B. Mullins, A Perspective on Protective Carbon Shells for Improved Stability of Alkaline Water Oxidation Electrocatalysts, *ACS Mater. Lett.*, 2024, **6**(8), 3190–3201, DOI: 10.1021/acsmaterialslett.4c00688.

56 I. S. Filimonenkov, C. Bouillet, G. Kéranguéven, P. A. Simonov, G. A. Tsirlina and E. R. Savinova, Carbon Materials as Additives to the OER Catalysts: RRDE Study of Carbon Corrosion at High Anodic Potentials, *Electrochim. Acta*, 2019, **321**, 134657, DOI: 10.1016/j.electacta.2019.134657.

57 C. Alegre, D. Sebastián and M. J. Lázaro, Carbon Xerogels Electrochemical Oxidation and Correlation with Their Physico-Chemical Properties, *Carbon*, 2019, **144**, 382–394, DOI: 10.1016/j.carbon.2018.12.065.

58 S. Pérez-Rodríguez, D. Sebastián and M. J. Lázaro, Electrochemical Oxidation of Ordered Mesoporous Carbons and the Influence of Graphitization, *Electrochim. Acta*, 2019, **303**, 167–175, DOI: 10.1016/j.electacta.2019.02.065.

59 T. Komatsu and T. Nakamura, Polycondensation/Pyrolysis of Tris-s-Triazine Derivatives Leading to Graphite-like Carbon Nitrides, *J. Mater. Chem.*, 2001, **11**(2), 474–478, DOI: 10.1039/b005982j.

60 Z. Q. Li, C. J. Lu, Z. P. Xia, Y. Zhou and Z. Luo, X-Ray Diffraction Patterns of Graphite and Turbostratic Carbon, *Carbon*, 2007, **45**(8), 1686–1695, DOI: 10.1016/j.carbon.2007.03.038.

61 J. R. Dennison, M. Holtz and G. Swain, Raman Spectroscopy of Carbon Materials, *Spectroscopy*, 1996, **11**(8), 38–45.
62 G. Pastore and M. P. Tosi, Electronic Structure of Liquids, in *Encyclopedia of Condensed Matter Physics*, Elsevier, 2024, pp. 161–170, DOI: 10.1016/B978-0-323-90800-9.00185-2.
63 R. L. McGreevy and L. Pusztai, The Structure of Molten Salts, *Proc. R. Soc. Lond. Ser. Math. Phys. Sci.*, 1990, **430**(1878), 241–261, DOI: 10.1098/rspa.1990.0090.
64 S. Roy, F. Wu, H. Wang, A. S. Ivanov, S. Sharma, P. Halstenberg, S. K. Gill, A. M. Milinda Abeykoon, G. Kwon, M. Topsakal, B. Layne, K. Sasaki, Y. Zhang, S. M. Mahurin, S. Dai, C. J. Margulis, E. J. Maginn and V. S. Bryantsev, Structure and Dynamics of the Molten Alkali-Chloride Salts from an X-Ray, Simulation, and Rate Theory Perspective, *Phys. Chem. Chem. Phys.*, 2020, **22**(40), 22900–22917, DOI: 10.1039/D0CP03672B.
65 R. E. Morris, Ionothermal Synthesis—Ionic Liquids as Functional Solvents in the Preparation of Crystalline Materials, *Chem. Commun.*, 2009, **21**, 2990, DOI: 10.1039/b902611h.
66 N. Díez, A. B. Fuertes and M. Sevilla, Molten Salt Strategies towards Carbon Materials for Energy Storage and Conversion, *Energy Storage Mater.*, 2021, **38**, 50–69, DOI: 10.1016/j.ensm.2021.02.048.
67 M. Thommes, K. Kaneko, A. V. Neimark, J. P. Olivier, F. Rodriguez-Reinoso, J. Rouquerol and K. S. W. Sing, Physisorption of Gases, with Special Reference to the Evaluation of Surface Area and Pore Size Distribution (IUPAC Technical Report), *Pure Appl. Chem.*, 2015, **87**(9–10), 1051–1069, DOI: 10.1515/pac-2014-1117.
68 S. Sharma, A. S. Ivanov and C. J. Margulis, A Brief Guide to the Structure of High-Temperature Molten Salts and Key Aspects Making Them Different from Their Low-Temperature Relatives, the Ionic Liquids, *J. Phys. Chem. B*, 2021, **125**(24), 6359–6372, DOI: 10.1021/acs.jpcb.1c01065.
69 S. Roy, M. Brehm, S. Sharma, F. Wu, D. S. Maltsev, P. Halstenberg, L. C. Gallington, S. M. Mahurin, S. Dai, A. S. Ivanov, C. J. Margulis and V. S. Bryantsev, Unraveling Local Structure of Molten Salts via X-Ray Scattering, Raman Spectroscopy, and *Ab Initio* Molecular Dynamics, *J. Phys. Chem. B*, 2021, **125**(22), 5971–5982, DOI: 10.1021/acs.jpcb.1c03786.
70 K. Gong, F. Du, Z. Xia, M. Durstock and L. Dai, Nitrogen-Doped Carbon Nanotube Arrays with High Electrocatalytic Activity for Oxygen Reduction, *Science*, 2009, **323**(5915), 760–764, DOI: 10.1126/science.1168049.
71 K. W. Pratt, Chronoamperometric Determination of Diffusion-Layer Thicknesses at Hydrodynamic Electrodes, *Anal. Chem.*, 1984, **56**(11), 1967–1970, DOI: 10.1021/ac00275a049.
72 M. Pimpilova, A Brief Review on Methods and Materials for Electrode Modification: Electroanalytical Applications towards Biologically Relevant Compounds, *Discov. Electrochem.*, 2024, **1**(1), 12, DOI: 10.1007/s44373-024-00012-8.

